



# Enhanced strength and ductility of AZ80 Mg alloys by spray forming and ECAP



Lingling Tang<sup>a</sup>, Yonghao Zhao<sup>a,\*</sup>, R.K. Islamgaliev<sup>b</sup>, Chi Y.A. Tsao<sup>c</sup>, R.Z. Valiev<sup>b,d</sup>, E.J. Lavernia<sup>e</sup>, Y.T. Zhu<sup>a,f</sup>

<sup>a</sup> Nano Structural Materials Center, School of Materials Science and Engineering, Nanjing University of Science and Technology, Nanjing 210094, China

<sup>b</sup> Institute of Physics of Advanced Materials, Ufa State Aviation Technical University, 12K. Marx St., Ufa, Russia

<sup>c</sup> Department of Materials Science and Engineering, National Cheng Kung University, 1 Ta Hsue Road, Tainan 701, Taiwan

<sup>d</sup> Laboratory for Mechanics of Bulk Nanomaterials, Saint Petersburg State University, 28 Universitetsky prospekt, Peterhof, Saint Petersburg 198504, Russia

<sup>e</sup> Department of Chemical Engineering and Materials Science, University of California, Irvine, CA 92697, USA

<sup>f</sup> Department of Materials Science & Engineering, North Carolina State University, Raleigh, NC 27695-7919, USA

## ARTICLE INFO

### Article history:

Received 29 April 2016

Received in revised form

10 June 2016

Accepted 12 June 2016

Available online 14 June 2016

### Keywords:

Mg alloy

Spray forming

ECAP

Strengthening

Deformation mechanisms

Ultra-fine grains

## ABSTRACT

The relatively low strength and poor ductility of conventional AZ80 Mg alloys have been attributed to the limited number of independent slip systems, in combination with the formation of fragile eutectic  $\beta$ -Mg<sub>17</sub>Al<sub>12</sub> networks at grain boundaries. In an effort to overcome these limitations, spray forming followed by equal channel angular pressing (ECAP) was employed to obtain a unique bi-modal microstructure: coarse grains were separated and surrounded by deformation networks consisting of ultrafine-grained Mg with an average grain size of 0.6  $\mu$ m and ellipsoidal shaped  $\beta$ -Mg<sub>17</sub>Al<sub>12</sub> particles with sizes of 200–300 nm. Tensile tests revealed the advantage of this structure: a yield strength of 235 MPa combined with an elongation to failure of 14%; the values are significantly higher than those of their conventional counterparts (100 MPa–12%, and 140 MPa–5%). The underlying strengthening and deformation mechanisms of this particular microstructure are discussed and analyzed.

© 2016 Elsevier B.V. All rights reserved.

## 1. Introduction

Mg alloys have potential for wide industrial applications, including those in the automobile and aviation industries as well as in 3C products (computer, communication and consumer electronic), because of their low density, high specific strength, high specific stiffness along with good machinability, recyclability and damping capacity. However, there are still several issues that limit their widespread industrial applications [1,2], one of which is their limited plasticity. Their hexagonal close-packed (hcp) crystal structure determines their limited independent slip systems, which is a major reason for their low plasticity. Other microstructural features may also significantly affect the plasticity. For example, in the AZ series of Mg alloys, which contain Al and Zn as solutes, continuous  $\beta$ -Mg<sub>17</sub>Al<sub>12</sub> precipitates usually form networks at grain boundaries (GBs) during casting. These  $\beta$ -Mg<sub>17</sub>Al<sub>12</sub> networks are fragile and tend to initiate cracks during subsequent deformation [3], which further lowers the limited plasticity. In addition, the eutectic  $\beta$ -Mg<sub>17</sub>Al<sub>12</sub> phase also behaves as a cathodic phase, which accelerates the corrosion of  $\alpha$ -Mg matrix [4].

It is well known that rapid solidification techniques such as spray forming can overcome some of the problems associated with conventional casting techniques. For examples, previous studies on aluminum and iron-based alloys prepared by spray forming [5–7] revealed significant reduction in grain size and micro-segregation, which consequently led to enhancement of mechanical properties. However, review of published studies [8,9] also shows that spray formed materials frequently contain a high volume fraction of pores which limit their ductility. Approaches to solve the porosity problem include extrusion, hot/cold roll or iso-static pressing, heat treatment, and forging following spray forming [10–13]. In reference [14], AZ91 prepared by spray forming and extrusion exhibited outstanding combinations of mechanical properties with a tensile ultimate strength (UTS) of 435 MPa, and YS of 360 MPa, and elongation to failure (EF) of 9.2%, whereas the hot-rolled AZ91 alloy [15] exhibited a UTS of 345 MPa and a YS of 297 MPa.

Severe plastic deformation (SPD) techniques, such as equal channel angular pressing (ECAP), have been effectively used to refine the overall microstructure of copper [16,17], aluminum [18], titanium [19], nickel [20], Mg [21] and other metals [22,23]. In the case of hcp metals such as Mg, ECAP processing has been reported to have the following effects. First, grain refinement; this is

\* Corresponding author.

E-mail address: [yhzhao@njjust.edu.cn](mailto:yhzhao@njjust.edu.cn) (Y. Zhao).

noteworthy because it is difficult to refine Mg grains to sub-micron level via traditional processing, such as rolling, forging and extrusion. However, ECAP processing has been used to effectively produce homogeneous ultrafine grained (UFG) microstructures in a number of commercial Mg alloys including AZ31, AZ61 and AZ91 [24–26]. It is known that the extent of grain refinement increases with the number of ECAP passes. Moreover, to successfully process pure Mg by ECAP, temperature of 400 °C is required; in the case of Mg-0.9% Al the required temperature is 200 °C [27]. These deformation temperatures are well above the recrystallization temperature ( $T_{\text{deformation}} > 0.4T_M$ ), which inevitably leads to dynamic recrystallization (DRX). It has been reported [28–30] that the reduced grain size of Mg alloys is a consequence of accumulated large strain and DRX.

Second, SPD techniques can break down secondary phases. For Mg alloys with high levels of Al, such as AZ80 and AZ91, a large volume fraction of  $\beta$ -Mg<sub>17</sub>Al<sub>12</sub> precipitates continuously and grows directly on the Mg base plane, which belongs to the space group of I43m and has long-plate morphology, thus resulting in ineffective age hardening. During ECAP, the distribution, morphology and size of the precipitates can be optimized for better performance [31–33]. Specifically, the breakdown and redistribution of the precipitates by ECAP processing can reduce fracture initiation during deformation, and thereby enhance plasticity. For example, the YS, UTS and EF of the AZ91 alloy [34] were remarkably increased to 290, 417 MPa and 8.45%, respectively, after a two-step ECAP processing, mainly due to the refinement of grain and Mg<sub>17</sub>Al<sub>12</sub> precipitates at GBs. Interestingly, several studies on Mg alloys [35–37] reported the presence of a bi-modal microstructure, that is CGs surrounded by a deformation layers near the original grain boundary that are composed of UFGs and a large numbers of second phase particles. Such a bi-modal microstructure has been reported to improve mechanical properties. For example [38], an ZK60 alloy processed by ECAP for 6 passes shows superplastic behavior with an elongation of 2040% at the tensile temperature of 473 K, which was attributed to the bi-modal structure with an area fraction of ~20% of large grains (20–50  $\mu\text{m}$ ) and ~80% of UFGs (~1  $\mu\text{m}$ ). Finally, SPD processing may modify the texture, which plays an important role in mechanical behavior of hcp metals. For example, ECAP processing and subsequent annealing have been reported to decrease the yield strength of an extruded AZ31 alloy due to texture modification [39]. A subsequent study by Lin et al. [40] found that the strength decrease was caused by the change of the Schmid factor due to tensile testing direction. The strong texture formation during the processing of Mg alloys may produce a strong anisotropy in mechanical properties [41].

A temperature step-down approach has been reported for ECAP processing of Mg alloys, in which lower processing temperature was used with increasing ECAP passes [42–44]. The advantage of this processing approach is that any DRX that occurs at higher temperatures effectively randomizes grain orientation and improves the plasticity for subsequent passes, while the lower temperatures at later passes generates a high defect density and fine grain sizes, which are beneficial to strength.

On the basis of the above published results, we hypothesize that it should be possible to implement a combination of ECAP and spray forming to simultaneously enhance the strength and ductility of Mg alloys. To verify this hypothesis, we processed an AZ80 Mg alloy by casting and spray forming and then ECAP processing via route Bc at various temperatures. Systematic microstructure studies on the extrusion direction (ED, X plane), flow direction (FD, Y plane) and longitudinal direction (LD, Z plane) were carried out. The Vickers microhardness and tensile properties were also determined. These experimental data were used to elucidate the underlying mechanisms that were responsible for the observed increase in strength and ductility.

**Table 1**

The chemical compositions (wt%) of AZ80 alloys in the present study.

Sample	Al	Zn	Mn	Cu	Si	Fe	Mg
As-sprayed	7.89	0.39	0.23	0.05	0.02	0.01	Bal.
As-cast	8.03	0.41	0.18	0.03	0.02	0.02	Bal.

## 2. Experimental procedures

### 2.1. Sample preparation

The initial CG AZ80 Mg alloys were prepared by conventional casting followed by a homogenization at 420 °C for 6 h to eliminate the massive coarse  $\beta$ -Mg<sub>17</sub>Al<sub>12</sub> network (hereafter, denoted as-cast) and by spray forming (hereafter, denoted as-sprayed). The chemical compositions of both as-cast and as-sprayed samples were determined by Inductively Coupled Plasma-Atomic Emission Spectrometry (Prodigy, American Leeman) and presented in Table 1. The ECAP processing procedure was: First, the as-sprayed and as-cast AZ80 samples were extruded at 300 °C with a rod diameter reduction from 20 mm to 16 mm. Second, the extruded rods were subjected to ECAP processing to six passes via the route Bc, in which the samples were rotated by 90° in the same direction between two consecutive passes (hereafter, denoted as as-sprayed-ECAP and as-cast-ECAP, respectively). Three ECAP temperatures of 350 °C, 250 °C and 200 °C were used in turn for two passes, respectively. After ECAP, samples parallel to the ED, FD and LD were sectioned from the rods. For comparison, pre-ECAP samples were also sectioned parallel to the ED from the as-cast and as-sprayed materials.

### 2.2. Microstructure characterization

Microstructure analyses were performed by means of optical microscopy (OM), scanning electron microscopy (SEM), transmission electron microscopy (TEM) and X-ray diffraction (XRD). The billets were ground with 800 and 1200 grit SiC abrasive paper and then mechanically polished using diamond slurries (3 and 1  $\mu\text{m}$ ) with oil-based medium. The polished specimens were finally etched at room temperature with a solution containing 2% oxalic acid and nitric acid 2% for 20 s. The OM and SEM observations were carried out at true color confocal microscope system (Axio CSM 700) and FEI, Quanta250 with energy dispersive spectrometer (EDS) detector of Oxford with an accelerating voltage of 20 kV. TEM specimens were first ground to a thin foil with a thickness of 60  $\mu\text{m}$ , dimpled to 30  $\mu\text{m}$ , and then milled to a thickness that is transparent to electron by precision ion milling (GATAN 691) with an Ar<sup>+</sup> accelerating voltage of 3.2 kV at room temperature. The TEM, high-resolution TEM (HREM) and scanning TEM (STEM) were performed using a FEI Techai G2 F30 microscope operating at 300 kV. Macroscopic phase identification by XRD was performed using a Bruker D8 Discover X-ray machine with Cu-K $\alpha$  radiation at 40 kV and 40 mA. Oxygen analysis of spray formed sample was conducted with X-ray Photoelectron Spectroscopy (XPS, ULVAC-PHI II, Japan) using a monochromatic Al K $\alpha$  source (15 kV, 45 W). Before XPS test, Ar ion sputtering was prepared for surface treatment, with ion gun voltage of 4 kV and gun angle of 45°. The whole XPS experiment was conducted under vacuum degree below  $5 \times 10^{-8}$  Torr and the lower limit of detection could reach zero point one percent (0.1 at%).

### 2.3. Mechanical properties

Vickers microhardnesses were measured on nano-indenter (HMV-G 21DT, Shimadzu) with a load of 980.7 mN and dwell time

of 10 s. Each Hv value was averaged from at least 25 data points with a standard deviation of  $\pm 2\%$ .

Tensile tests were carried out at room temperature with an initial quasi-static strain rate of  $1 \times 10^{-3} \text{ s}^{-1}$ . The strain was measured by calculation of crosshead movement using computer software. Flat dog-bone shaped tensile specimens with gauge dimensions of  $1 \times 1 \times 4 \text{ mm}^3$  were sectioned by electro spark machining from the central regions of the round bars with the gauge axis parallel to the ED. Each tensile test result was repeated 3 times to assure the reproducibility of the data.

### 3. Experimental results

#### 3.1. Microstructures

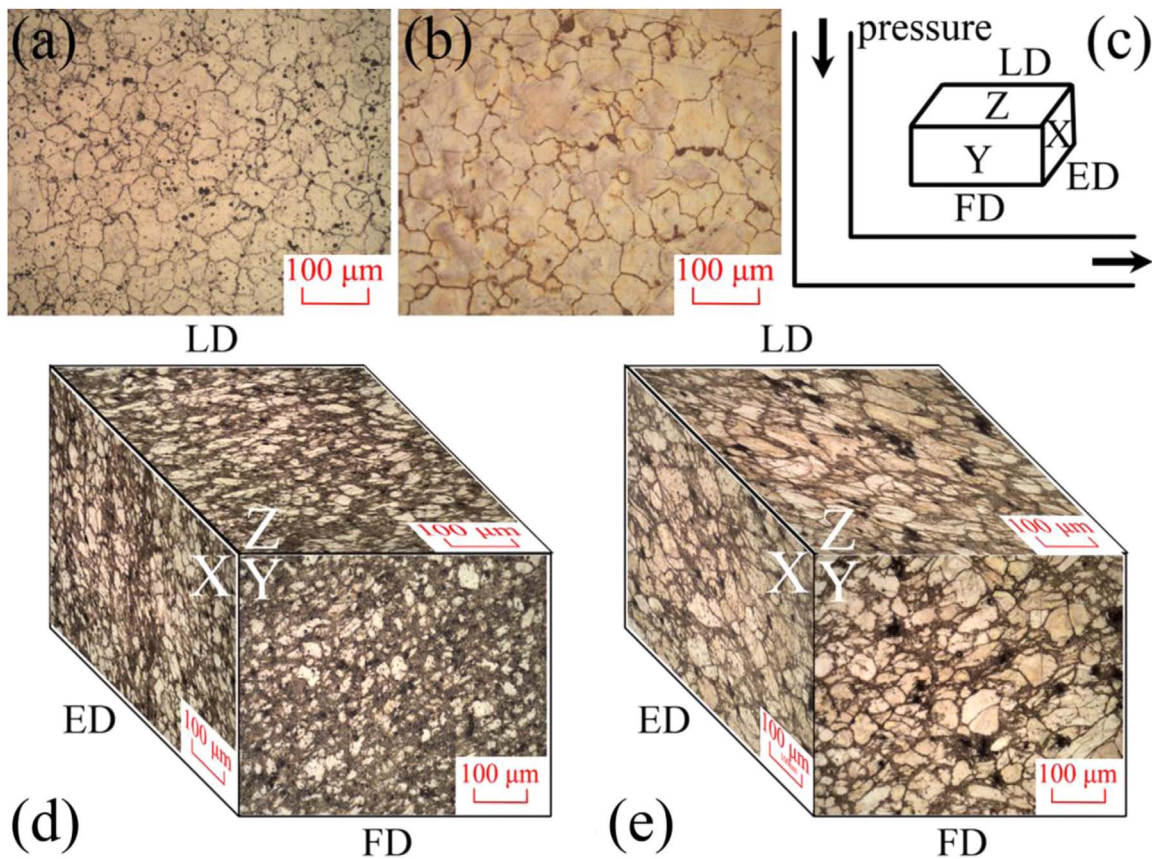
The OM observations on the original as-sprayed and as-cast samples are shown in Fig. 1(a) and (b). The grain size of the as-sprayed and as-cast samples are approximately 40 and 60  $\mu\text{m}$ , respectively, measured using the average linear intercept method. In the as-sprayed sample, there are large precipitates with a diameter of several micrometers and some smaller particles at both GBs and grain interiors. For the as-cast sample, most large precipitates are located at the GBs. Overall, the spray forming produced finer microstructures than traditional casting.

Fig. 1(d) and (e) depicts the OM images of the as-sprayed-ECAP and as-cast-ECAP samples, respectively, in different directions of ED, FD and LD. Both samples exhibit a structure feature where coarse Mg grains were separated and surrounded by deformation networks. The sizes of the coarse-grains range from 20 to 30  $\mu\text{m}$  in the as-sprayed-ECAP samples and from 40 to 50  $\mu\text{m}$  in the as-cast-

ECAP sample; these grain sizes are significantly smaller than those samples that were not processed via ECAP. The amount and size of the large precipitates with diameters of several micrometers observed in samples without ECAP appear to remain unchanged following ECAP, suggesting that ECAP did not break up these large precipitates.

The SEM images of the as-sprayed and as-cast samples are shown in Fig. 2(a) and (b). The SEM results confirmed microstructure characteristics observed by OM (Fig. 1(a) and (b)): precipitates formed at GBs and in grain interiors for the as-sprayed sample, but primarily at GBs for the as-cast sample. In addition,  $\beta\text{-Mg}_{17}\text{Al}_{12}$  precipitated at the GBs to form almost continuous networks for both as-sprayed and as-cast samples. Fig. 2(c)–(h) displays six individual SEM images viewed from different directions of two specimens: Images c, e and g are for ED, FD and LD of as-sprayed-ECAP sample, and d, f and h for ED, FD and LD of as-cast-ECAP sample. A bi-modal microstructure can be seen: CG Mg grains were separated and surrounded by deformation networks with UFGs. This microstructure can also be regarded as large soft grains embedded in harder UFG matrix, similar to the “harmonic structure” reported earlier [45]. In addition, there exists white ellipsoidal particles approximately 10–30  $\mu\text{m}$  within the deformed layer. This is more clearly seen in Fig. 3(a) and (b) for the as-sprayed-ECAP sample in ED with larger magnifications. The ellipsoidal shaped particles have sizes in the range of 200–300 nm. Moreover, a few larger polygon-shaped particles several micrometers in size can be seen in the vicinity of the agglomerated ultrafine particles.

To determine the compositions of ultrafine and coarse particles, we performed element point scanning with EDS, and results are shown in Fig. 3(c) and (d) for the particles labeled by A and B. The EDS results suggest that the ultrafine particles are the  $\beta\text{-Mg}_{17}\text{Al}_{12}$



**Fig. 1.** Optical micrograph (OM) of (a) as-sprayed, (b) as-cast AZ80 alloys; (c) schematic of sectioned samples corresponding to the ECAP-processed billet; OM of (d) as-sprayed-ECAP and (e) as-cast-ECAP AZ80 alloys observed from the ED (X plane), FD (Y plane) and LD (Z plane). The ED, FD and LD here indicate for the extrusion direction, flow direction and longitudinal direction, respectively.

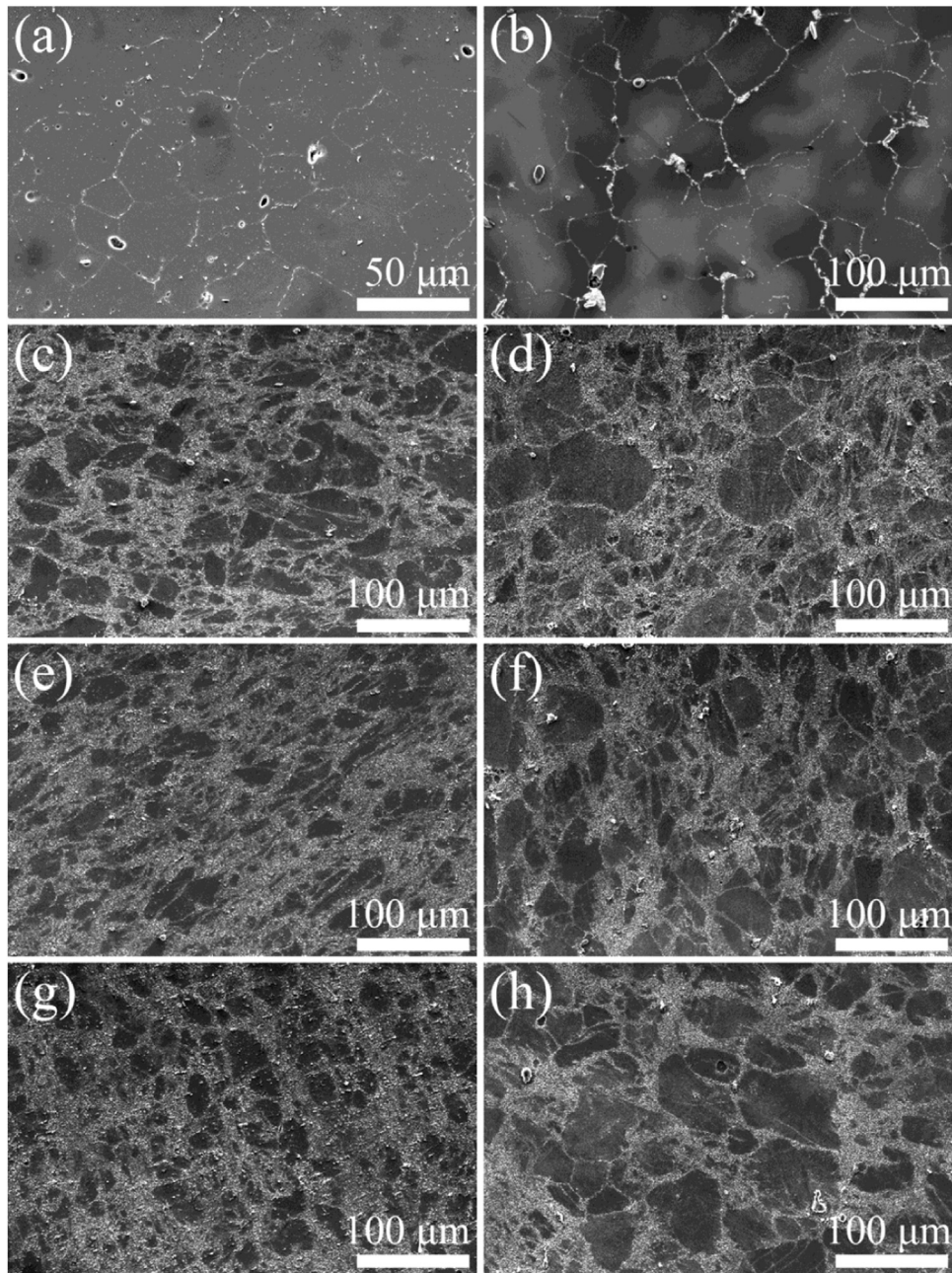


**Fig. 2.** SEM images of (a) as-sprayed, (b) as-cast AZ80 alloys, and the as-sprayed-ECAP (c, e and g) as well as the as-cast-ECAP (d, f and h) AZ80 alloys along the ED (c, d), FD (e, f) and LD (g, h).

phase and that the coarse particles are likely the intermetallic compound with chemical formula of  $\text{Al}_8\text{Mn}_5$ . Similar results have also been reported [47,48]. In addition, we further performed Mg, Al and Mn elemental mapping in the area C highlighted with a red rectangle in Fig. 3(b), as shown in Fig. 3(e). These results reveal that the coarse particle contains both Al and Mn. From over 30 similar SEM images shown in Fig. 2(c)–(h), the volume fraction of  $\beta\text{-Mg}_{17}\text{Al}_{12}$  phase was calculated through pixel dots by Image Pro Plus professional software and was determined to be 16% for the as-sprayed-ECAP and 13% for the as-cast-ECAP samples. In the discussion on mechanical behavior that follows, we do not take into account the  $\text{Al}_8\text{Mn}_5$  phase, given their large sizes and small volume fraction. XRD analyses confirm the presence of  $\beta\text{-Mg}_{17}\text{Al}_{12}$  and  $\text{Al}_8\text{Mn}_5$  (see Fig. 4). In addition, after ECAP, the corresponding  $\beta\text{-Mg}_{17}\text{Al}_{12}$  peak height dramatically increased, which indicates that ECAP promoted the precipitation of a large number of

$\text{Mg}_{17}\text{Al}_{12}$  particles from the  $\alpha\text{-Mg}$  matrix.

To further study the microstructure within the deformed UFG networks, TEM observations were carried out. Fig. 5 presents the TEM images of AZ80 alloys in ED, FD, and LD of as-sprayed-ECAP (a, c, e) and as-cast-ECAP (b, d, f) samples. The white arrows and black arrows highlight the  $\alpha\text{-Mg}$  grains and  $\beta\text{-Mg}_{17}\text{Al}_{12}$  particles, respectively. It is evident that the UFG  $\alpha\text{-Mg}$  grains were formed after ECAP: the average grain size is 0.6 and 0.8  $\mu\text{m}$  for the as-sprayed-ECAP and as-cast-ECAP samples, respectively, as measured from over 200 grains for each direction in TEM micrographs. The insets in Fig. 5(a) and (b) are their corresponding selected area diffraction patterns (SADP). They show evident diffraction spots, indicating a texture among the UFGs. Moreover, ellipsoidal shaped  $\beta\text{-Mg}_{17}\text{Al}_{12}$  particles with sizes ranging from several tens to hundreds of nanometers were observed, as marked by the black arrows. It is difficult to locate any complete  $\alpha\text{-Mg}$  grain in the Fig. 5

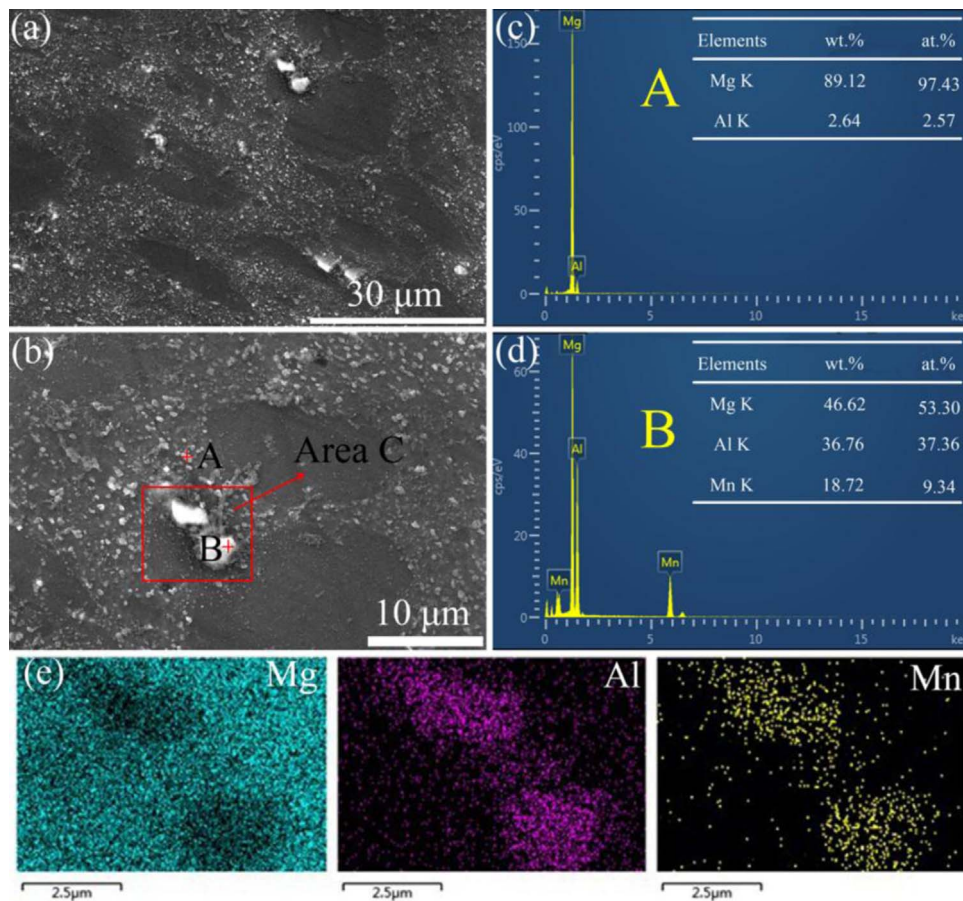


**Fig. 3.** SEM images of (a) as-sprayed-ECAP sample in the ED and (b) high-magnification image of  $\beta$ - $Mg_{17}Al_{12}$  (marked as "A") and  $Al_8Mn_5$  (marked as "B") particles in image (a); (c) and (d): elemental spectrums provided by EDS in point scan mode and elemental concentrations in wt% and at% for particle A and B. (e) Elements Al, Mg and Mn map scan of  $Al_8Mn_5$  particles in area C marked in image (b). (For interpretation of the references to color in this figure legend, the reader is referred to the web version of this article.)

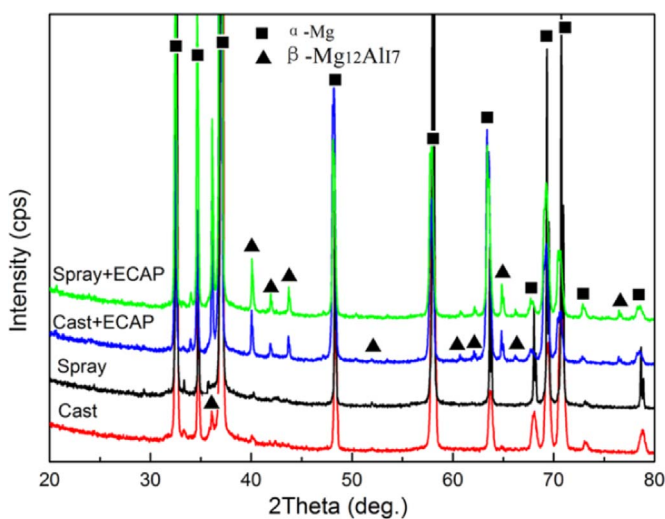


**Fig. 4.** The XRD of the as-sprayed, as-cast, as-sprayed-ECAP and as-cast-ECAP AZ80 alloys.

(d) and (f). It is speculated that those images were taken from the CG region or transition region of the bi-modal structure. The micrograph in Fig. 6, obtained from the FD of as-cast-ECAP sample, clearly shows the bi-modal structure. The CGs with the size of  $30\ \mu m$  were surrounded by an UFG region with a width of  $10\ \mu m$  corresponding to the deformation UFG layer as seen in SEM images (Fig. 2).

Higher-magnification TEM images of matrix grains in ED of as-sprayed-ECAP and as-cast-ECAP are shown in Fig. 7(a) and (b). HREM images are shown in Fig. 7(c) and (d), corresponding to the white solid line circled region in Fig. 7(a) and (b), respectively. The calibrated diffraction pattern insets are the corresponding Fourier transformation (FFT) patterns of the HREM images. There are three pairs of parallel lattice planes in the diffractogram. The corresponding inverse FFT pattern of one pair of parallel lattice planes is displayed in Fig. 7(e) and (f), the  $(1\ \bar{1}\ 0\ 1)$  and  $(1\ 0\ \bar{1}\ 0)$  planes for the as-sprayed-ECAP and as-cast-ECAP, respectively. In Fig. 7(e) and (f), dislocations were marked with "L" in red, at the points where the extra atomic planes terminate. In order to quantify dislocation density, the numbers of dislocation per unit area were calculated, based on more than thirty images. The calculated numbers of dislocations per unit area are  $2.1 \times 10^{13}$  and  $1.1 \times 10^{13}$  for the as-sprayed-ECAP and as-cast-ECAP specimens, respectively, as summarized in Table 2.

Fig. 8(a) illustrates TEM bright-field image of the matrix and the  $\beta$ - $Mg_{17}Al_{12}$  particle in ED of as-sprayed-ECAP sample. The calibrated diffraction pattern of  $\beta$ - $Mg_{17}Al_{12}$  phase shows that these images were taken with electron beam in direction of  $[0\ 0\ 0\ 1]$ , just parallel to the  $c$  axis of  $\alpha$ -Mg grain. The corresponding HREM image of the red rectangle region is shown in Fig. 8(b). The interplanar spacing of the Mg matrix and the second phase were measured to be  $0.243\ nm$  and  $0.248\ nm$ , which refer to the  $(1\ \bar{1}\ \bar{2}\ 0)$  and  $(4\ 1\ 1)$  lattice planes, respectively. In addition, the interface between the second phase and the matrix is smooth and the GBs could be barely observed. According to a previous study [46], the two predominant orientation relationships (ORs) between the  $\beta$ -

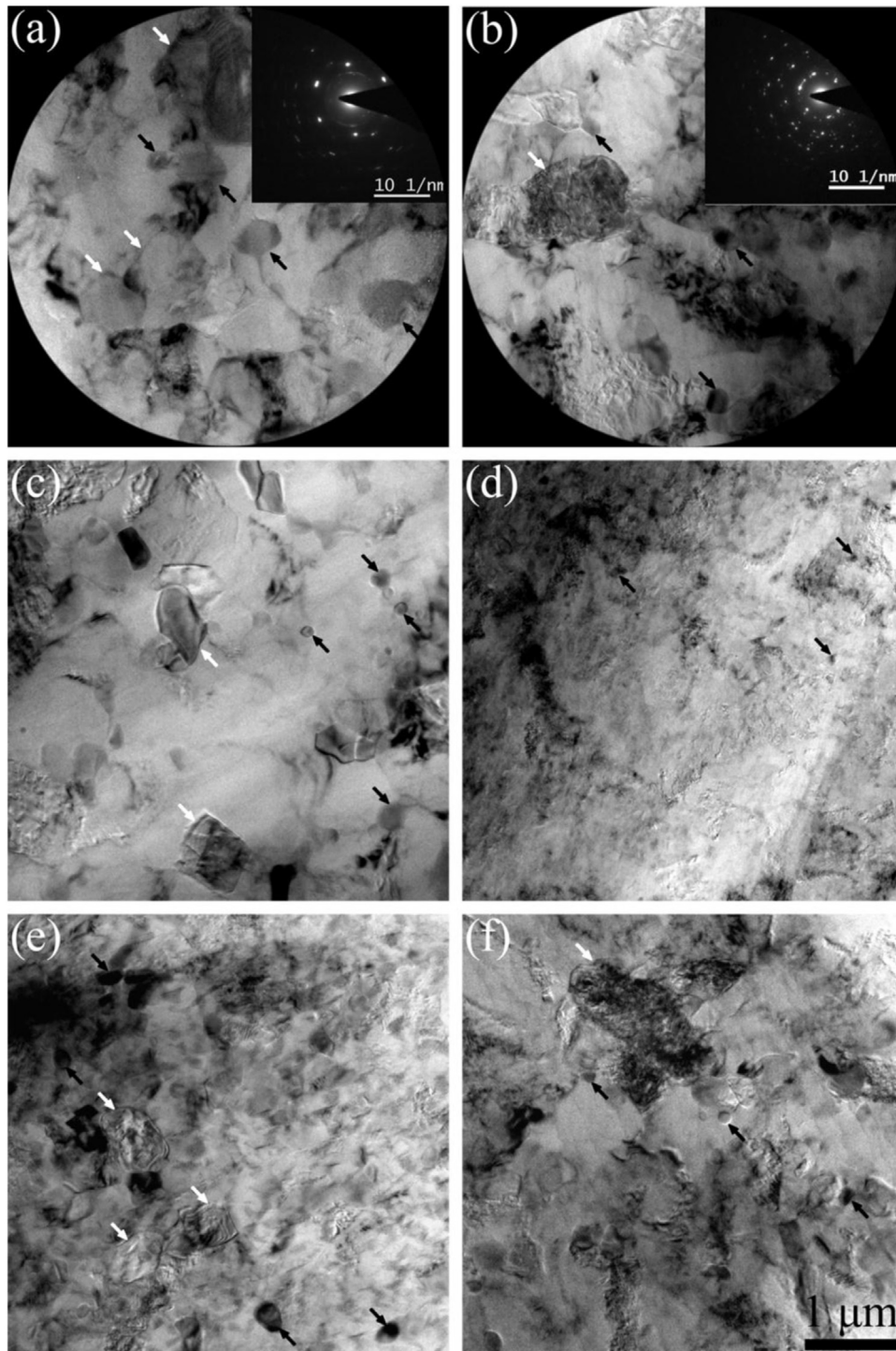


**Fig. 5.** TEM bright field micrographs in the ED (a,b), FD (c,d) and LD (e,f) of as-sprayed-ECAP (a, c and e) and as-cast-ECAP (b, d and f) samples; the insets within (a) and (b) are their corresponding SADPs; the white arrows refer to  $\alpha$ -Mg grains and the black arrows point to  $\beta$ -Mg<sub>17</sub>Al<sub>12</sub> particles.

phase and Mg matrix are  $(0\ 0\ 0\ 1)_m // (1\ \bar{1}\ 1)_p$ ,  $[1\ \bar{2}\ 1\ 0]_m // [1\ \bar{1}\ \bar{2}]_p$  and  $(1\ \bar{2}\ 1\ 1)_m // (1\ 1\ 0)_p$ ,  $[1\ 0\ \bar{1}\ 0]_m // [1\ 1\ 0]_p$ , both of which are incoherent interfaces. However, similar findings of  $(4\ 1\ 1)$  lattice planes have been reported in spray-formed AZ31 [47], raising a speculation as to whether this observation is characteristic of the spray formed materials; work in this area is continuing. The STEM images shown in Fig. 9(a) and (b) were taken from the  $\beta$ -Mg<sub>17</sub>Al<sub>12</sub> particles present in ED of the as-sprayed-ECAP and as-cast-ECAP specimens, respectively. The average particle sizes are about 240 and 300 nm, respectively. Results from extensive statistical

analyses of microstructure characteristics are summarized in Table 2, including the average Mg grain size in the ED (0.62 and 0.73  $\mu\text{m}$ ), FD (0.50 and 0.91  $\mu\text{m}$ ) and LD (0.76 and 0.82  $\mu\text{m}$ ) for the as-sprayed-ECAP and as-cast-ECAP specimens.

### 3.2. Mechanical properties

The results of microhardness measurements are summarized in Table 3. ECAP dramatically increased the microhardness of the original as-sprayed and as-cast samples. In both as-sprayed-ECAP

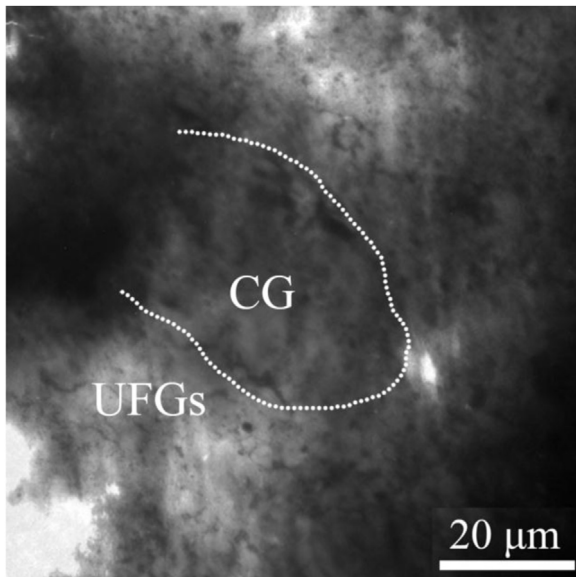


**Fig. 6.** TEM micrograph showing a microstructure with a large grain embedded in the UFG matrix as observed in the FD of the as-cast-ECAP sample.

and as-cast-ECAP samples, highest HV values appear in the FD, followed by samples in ED and then LD, which is consistent with the mechanical properties of ECAP-processed AZ31B alloy [41]. However, the outstanding mechanical properties of samples in FD was attributed to twinning-dominated mechanism, which rarely occurs in UFG Mg alloys [48,49]. Additionally, the incremental grain refinement using the temperature step-down method has been reported to suppress twinning [44]. Our TEM investigation failed to identify deformation twins in our UFG Mg alloys, which are consistent with the literature.

The engineering true stress-strain curves of the as-cast, as-sprayed, and ECAPed samples along the extrusion direction (in Y plane) are shown in Fig. 10. Table 4 lists the YS, UTS and EF (ductility, elongation to failure) of all samples. The data show that the EF of the as-sprayed sample (5%) is much smaller than that of the as-cast sample (12%), which is likely due to the presence of porosity in the as-sprayed material. While the YS of the as-sprayed sample (140 MPa) is higher than that of the as-cast sample (100 MPa), consistent with its finer grains and precipitate, as shown in Fig. 1. After further ECAP processing, both YS and EF are improved significantly for both the as-sprayed and as-cast samples. For example, the YS and EF of the as-cast sample were increased to 200 MPa and 14%, respectively, by ECAP; and those of the as-sprayed sample to 235 MPa and 14%, respectively. In other words, the combination of spray forming and ECAP process achieved the best YS and EF properties (235 MPa and 14%). As discussed later, these superior mechanical properties are associated with the unique microstructure formed by ECAP.

### 3.3. Oxygen analysis

During the spray forming process, oxygen is generally present, and therefore oxide phases will form. In order to evaluate oxygen concentration in the as-sprayed sample, ion sputtering and XPS were carried out. As shown in Fig. 11(a), the atomic concentration of Mg and O varies with sputter time. Sputtering for 4 min decreased atomic concentration of O from 36.2% to 0% while the atomic concentration of Mg increased from 16.8% to 100%, and the atomic concentration remained constant during further sputtering. This suggests that the surface oxidation layer was removed

totally after sputtering for 4 min. In order to understand the variation of atomic concentration of Mg and O during sputtering, point scanning with beam spot of 200 μm was conducted every minute within sputter time of 4 min, as shown in Fig. 11(b) and (c). Narrow band spectrum of Mg 2s is shown in Fig. 11(b), it can be seen that only one peak with a binding energy ( $P_{BE}$ ) of about 89 eV appeared at 1 min, while at two minutes another peak appeared ( $P_{BE}=102$  eV) and it remained basically unchanged with sputter time prolonged to 4 min. In Fig. 11(c) of narrow band spectrum of O 1s, there is a peak with  $P_{BE}=532$  eV at 1 min and this peak disappeared when prolonged to 2 min. From 2 min to 4 min, the three curves almost remain unchanged. When the sample was sputtered for 5 min, it was scanned again in point mode. The narrowband spectrum of Mg 2s (Fig. 11(d)) shows the same peak position as in the 4-min sputtering (Fig. 11(b)). For narrow band spectrum of O 1s shown in Fig. 11(e), no obvious peaks could be found, which means that the O concentration is lower than the detection limit of XPS.

Based on Mg and O standard spectra for XPS analysis,  $P_{BE}=89$  eV corresponds to Mg,  $P_{BE}=102$  eV to  $Mg^{2+}$ , and  $P_{BE}=532$  eV to  $O^{2-}$ . These results indicates that 1) there were negligible oxides (below 0.1 at%) formed during spray forming; 2) the valence states of Mg and  $Mg^{2+}$  confirm that Mg exists in  $\alpha$ -Mg and  $\beta$ - $Mg_{17}Al_{12}$  phase, which is consistent with SEM and TEM results. As for as-sprayed-ECAP sample, the as-sprayed sample has negligible oxides and ECAP processing will not introduce O, so the effect of oxides could also be negligible.

## 4. Discussion

### 4.1. Microstructure-property relationship

To compare with the tensile results of AZ80 alloys in this study, a large number of previous studies [26,27,39,40,50–67] on tensile properties at room temperature for AZ series Mg alloys processed by ECAP were summarized in Fig. 12. Clearly, the YS and EF follows an often-observed trend of strength-ductility trade-off: i.e., high strength accompanied with low ductility, and vice versa. Specifically, with the increasing solute concentration from AZ31 to AZ91, the YS increases and the EF decreases. For instance, the AZ31 alloys provide the best plastic deformation ability with an EF of 60% and a YS of 170 MPa [41], while the AZ91 alloys possess a high YS of  $\sim 300$  MPa and an EF of  $\sim 9\%$  [48]. Moreover, AZ31 alloy could have a high YS of 372 MPa and a low EF of 1% by ECAP grain refinement. The present tensile results obtained for the as-sprayed-ECAP and as-cast-ECAP AZ80 samples also follow the same trends in the literature data. In addition, the as-sprayed-ECAP shows the best properties among reported AZ80 alloys.

The observed simultaneous improvement of strength and ductility of the Mg alloys by ECAP processing can be primarily attributed to their unique structure, which is similar to the bimodal “harmonic structure” formed by consolidation of severe plastically deformed powders [45]. Such a microstructure is characterized by soft CG domains embedded in continuous strong UFG network matrix. Simultaneous increase in both strength and ductility is typically observed for such a structure. It is also to some extent similar to the heterogeneous structure reported in Ti, which has been reported to have the strength of the UFG Ti and ductility of CG Ti [68]. This type of structure is found to produce high back stress and back stress hardening, which improves both the yield strength and ductility. The back stress evolution during a tensile test can be measured by the approach of unloading-reloading at varying tensile strains [69]. The back stress in the present Mg alloy samples will be further studied.

The dispersed distribution of  $\beta$ - $Mg_{17}Al_{12}$  particles in the

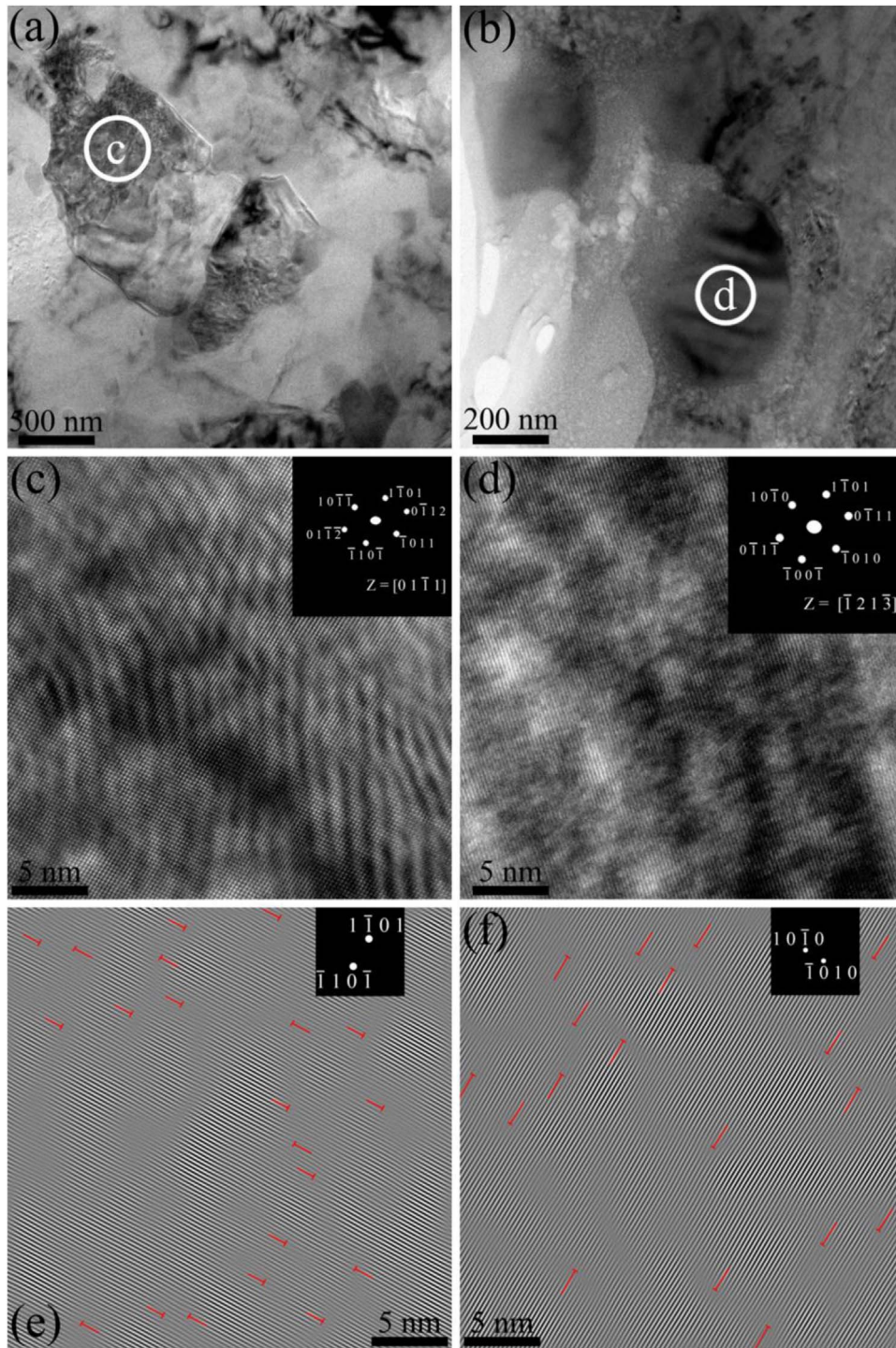


**Fig. 7.** TEM bright field micrographs of  $\alpha$ -Mg grains in the ED of the as-sprayed-ECAP (a) and the as-cast-ECAP (b) samples; (c) and (d): HREM images of white solid line circle area in images (a) and (b), the insets of diffraction patterns are the corresponding FFT of images (c) and (d); (e) and (f) Inverse FFT of  $(1 \bar{1} 0 1)$  and  $(1 0 \bar{1} 0)$  lattice planes of (c) and (d) for the as-sprayed-ECAP and the as-cast-ECAP samples. The edge dislocations are highlighted by red " $\perp$ " symbols. (For interpretation of the references to color in this figure legend, the reader is referred to the web version of this article.)

UFG deformation layer should also have played an important role in the mechanical behavior. It is known that strengthening and toughening can be obtained through dispersed hard particles to interact with dislocations or grain boundaries. For example, tensile properties have been reported improved by adding  $\text{La}_2\text{O}_3$  particles in molybdenum alloys [70]. The  $\text{Mg}_{17}\text{Al}_{12}$  particles in AZ80 alloy may have the same effect. Though  $\text{Mg}_{17}\text{Al}_{12}$  particles were normally reported to precipitate along the original

grain boundaries [29], their formation mechanism within deformation layers is still not clear. Zhao et al. proposed that ECAP process could accelerate precipitation in UFG 7075 Al alloy [71]. Thus, it is speculated that the formation of so many  $\text{Mg}_{17}\text{Al}_{12}$  particles may come from two ways: new precipitation or the fracture and redistribution of original large network-shaped  $\beta$ -phase.

#### 4.2. Strengthening factors

The relationship between microstructure and properties has been discussed in Section 4.1. In order to further shed light on the relationship, the responding values of (I) grain refinement, (II) solid solution, (III) second phase, and (IV) dislocations are estimated in this section. It should be noted that these are only qualitative estimations, and the interaction between these factors are highly possible but is not considered.

Generally, grain refinement strengthening can be described by the Hall-Petch equation

$$\sigma_{hp} = \sigma_0 + kd^{1/2} \quad (1)$$

For the ECAP-processed AZ80 alloys with bi-modal structure here, based on the mixture rule, it can be rewrote to

$$\sigma_{hp} = \sigma_0 + xk/\sqrt{d_{CG}} + (1-x)k/\sqrt{d_{UFG}} \quad (2)$$

where  $\sigma_0$  of pure Mg is about 11 MPa [72];  $k$  is a constant, which is  $0.28 \text{ MNm}^{-3/2}$  for Mg [73];  $d$  in Eq. (1) is  $40 \mu\text{m}$  and  $60 \mu\text{m}$  for as-sprayed and as-cast samples;  $d_{CG}$  and  $d_{UFG}$  in Eq. (2) are the average grain size of CG and UFG  $\alpha$ -Mg phase, using the values of  $25 \mu\text{m}$  and  $45 \mu\text{m}$  for  $d_{CG}$ ,  $0.6 \mu\text{m}$  and  $0.8 \mu\text{m}$  for  $d_{UFG}$  in the as-sprayed-ECAP and as-cast-ECAP samples, respectively;  $x$  represents for the area fraction of UG  $\alpha$ -Mg phase, which can be

**Table 2**

Results from extensive statistical analyses of microstructure characteristics of the as-sprayed-ECAP and as-cast-ECAP samples: average size of  $\alpha$ -Mg grains  $d_1$  and  $\beta$ - $\text{Mg}_{17}\text{Al}_{12}$  particles  $d_2$  and the numbers of dislocation per unit area  $\rho_{ds}$ .

	As-sprayed-ECAP			As-cast-ECAP		
	ED	FD	LD	ED	FD	LD
$\bar{d}_1$ ( $\mu\text{m}$ )	0.62	0.50	0.76	0.73	0.91	0.82
$\bar{d}_2$ ( $\mu\text{m}$ )		0.24			0.30	
$\bar{\rho}_{ds}$ ( $/\text{m}^2$ )		$2.1 \times 10^{13}$			$1.1 \times 10^{13}$	

**Table 3**

Hv0.1 microhardness values of the as-sprayed, as-cast, as-sprayed-ECAP and as-cast-ECAP samples. The dwell time is 10 s, each value was averaged from 25 data with an uncertainty of  $\pm 2\%$ .

	ED	FD	LD
As-sprayed	64		
As-cast	57		
As-sprayed-ECAP	115	127	112
As-cast-ECAP	104	117	103

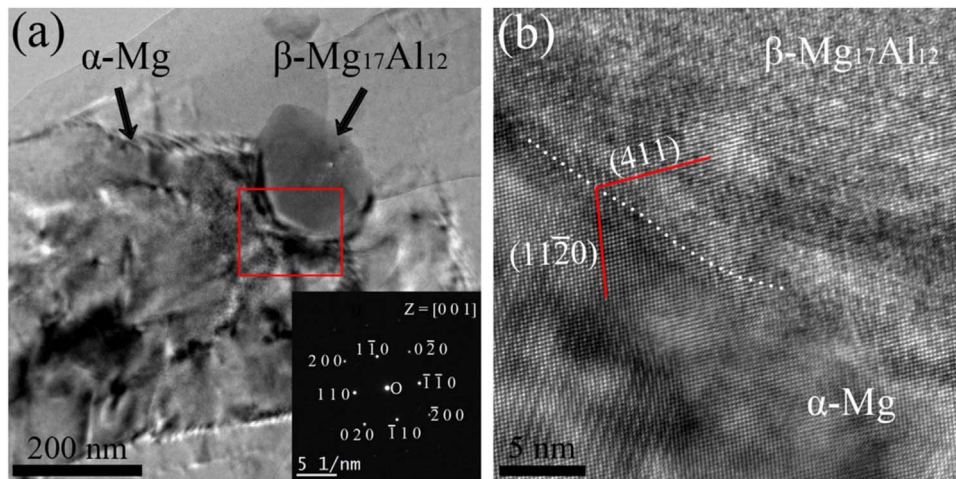


**Fig. 8.** (a) TEM micrograph of  $\alpha$ -Mg and  $\beta$ - $\text{Mg}_{17}\text{Al}_{12}$  particles in the ED of the as-sprayed-ECAP sample, the inset shows the corresponding diffraction pattern of  $\beta$ - $\text{Mg}_{17}\text{Al}_{12}$  particle; (b) HREM image of the red rectangular region in image (a). (For interpretation of the references to color in this figure legend, the reader is referred to the web version of this article.)

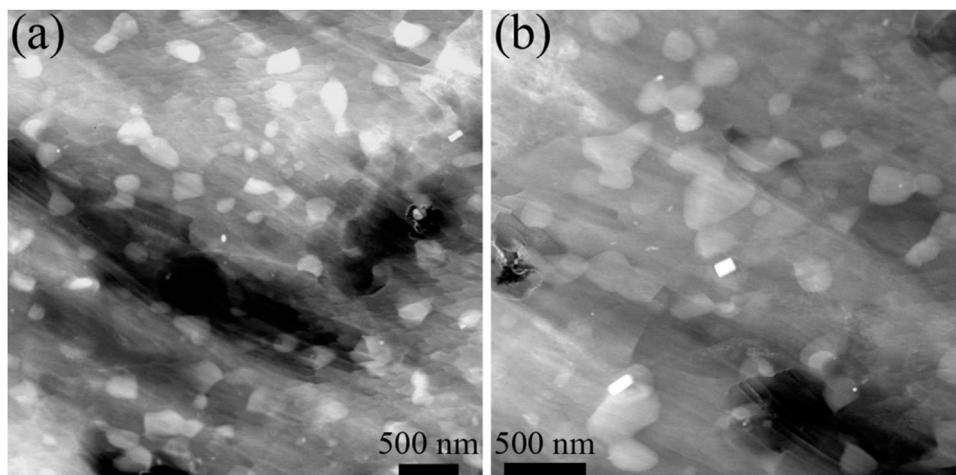


**Fig. 9.** The STEM micrographs of  $\beta$ - $\text{Mg}_{17}\text{Al}_{12}$  particles in the ED of (a) the as-sprayed-ECAP and (b) the as-cast-ECAP samples.

expressed by  $d_{CG}^2/4\tau_{UFG}(d_{CG} + \tau_{UFG})$ ,  $\tau_{UFG}$  is the average thickness of deformation layer and 20  $\mu\text{m}$  and 10  $\mu\text{m}$  for the as-sprayed-ECAP and as-cast-ECAP samples, respectively, according to the calculation from SEM micrographs. Therefore, grain refinement

strengthening contributions are about 55, 47, 87 and 76 MPa for the as-sprayed, as-cast, as-sprayed-ECAP and as-cast-ECAP samples, respectively.

Solid solution strengthening occurs as a consequence of the interactions between moving dislocations and the strain fields associated with misfit solute atoms, and can be expressed by [74].

$$\sigma_{ss} = \sigma_0 + \frac{3 \cdot 1\epsilon G C^{1/2}}{700} \quad (3)$$

where  $\epsilon$  is an experimental constant, which is 0.22 for Mg-Al series alloys [72];  $G$  is the shear modulus, which is  $1.66 \times 10^4$  MPa for Mg [73];  $C$  is the solute concentration in atomic percentage. For as-sprayed and as-cast samples, it is speculated that Al and Zn

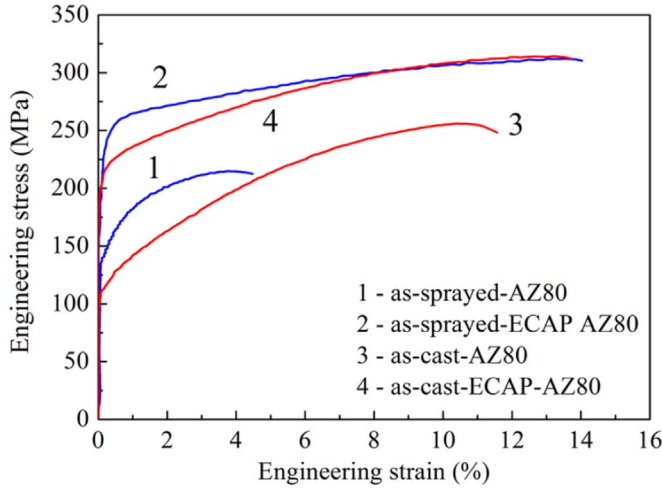


Fig. 10. The engineering stress-true strain curves of the as-sprayed, as-cast, as-sprayed-ECAP and as-cast-ECAP AZ80 Mg alloys along the extrusion direction.

Table 4  
Tensile properties for AZ80 alloy at room temperature: the ultimate tensile strength (UTS), yield strength (YS) and elongation to failure (EF).

	As-sprayed	As-sprayed-ECAP	As-cast	As-cast-ECAP
YS (MPa)	140	235	100	200
UTS (MPa)	225	305	255	315
EF (%)	5	14	12	14

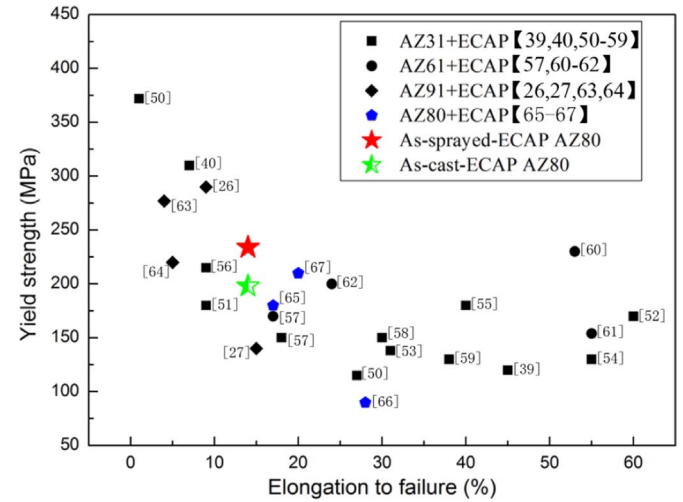


Fig. 12. The yield strength versus ductility at room temperature for AZ series Mg alloys (AZ31, AZ61, AZ91 and AZ80 alloys) processed by ECAP.

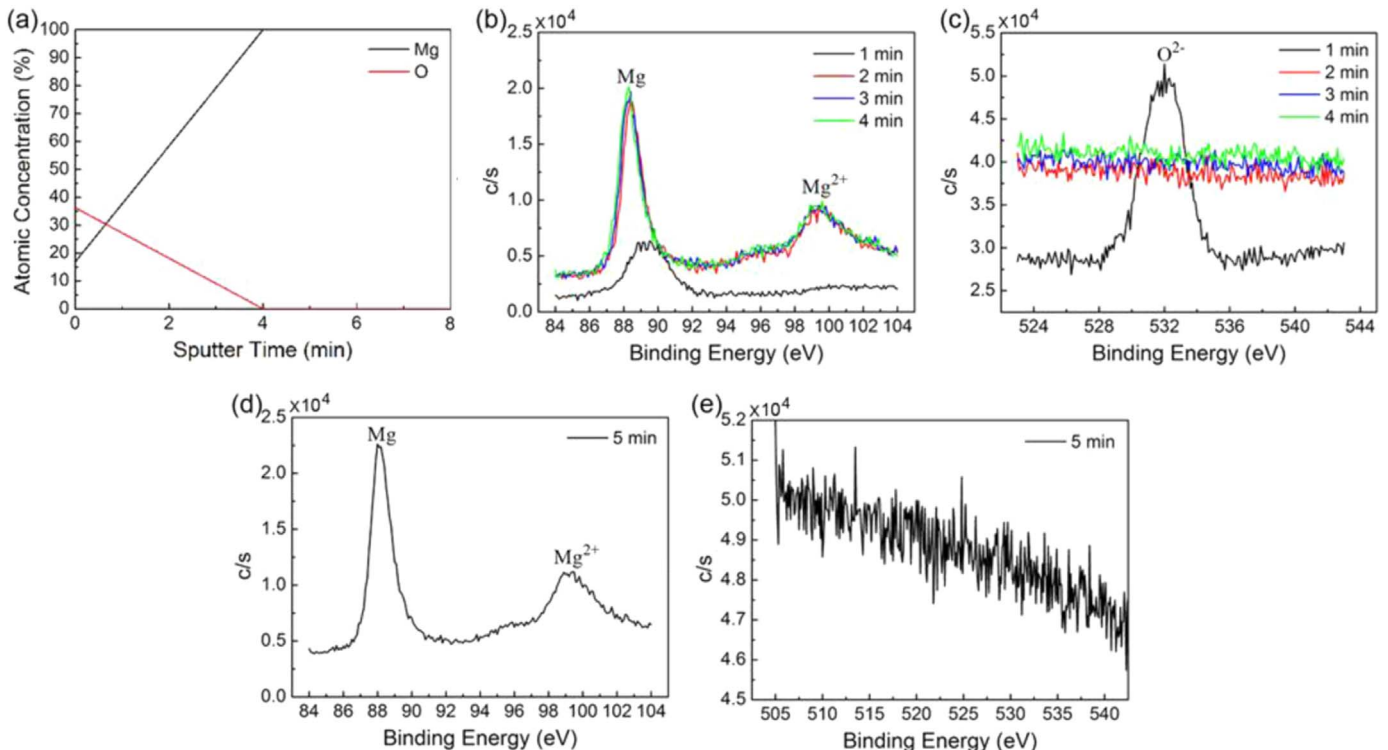


Fig. 11. Ion sputtering and XPS results in as-sprayed sample: (a) atomic concentration of Mg and O versus sputter time; narrow band spectrum of (b) Mg 2s and (c) O 1s at sputter time of 1 min, 2 min, 3 min and 4 min; narrow band spectrum of (d) Mg 2s and (e) O 1s at sputtering for 5 min.

**Table 5**  
Relative contributions of different strengthening mechanisms to the yield strength (YS) of the AZ80 alloy (unit: MPa). The data in brackets show percentage of the contributions.

	Fine grain strengthening	Solid solution strengthening	Second phase strengthening	Dislocation strengthening	Theoretical YS	Tensile YS
As-sprayed	55	56	0	0	111	140
As-cast	47	56	0	0	103	100
As-sprayed-ECAP	87	43	88	21	239	235
As-cast-ECAP	76	43	70	16	205	200
$\Delta_{\text{as-sprayed-ECAP-as-sprayed}}$	32(+21%)	−13(−8%)	88(+57%)	21(+14%)		
$\Delta_{\text{as-cast-ECAP-as-cast}}$	29(+23%)	−13(−10%)	70(+55%)	16(+13%)		

solute were totally dissolved into Mg matrix and the surplus of Al and Zn addition is 7.6 at%. In the ECAP-processed samples, the solid solution strengthening contribution decreases due to the fact that the matrix is depleted of solute as the  $\beta$ -Mg<sub>17</sub>Al<sub>12</sub> precipitation process proceeds. According to Mg-Al and Mg-Zn binary phase diagram at temperature of 200 °C (the final ECAP processing temperature), the surplus of Al and Zn addition is 4.1 at%. Finally, for as-sprayed (as-cast) and as-sprayed-ECAP (as-cast-ECAP), increase of YS resulted from solid solution strengthening is 56 MPa and 43 MPa.

The second-phase particle strengthening can be estimated by the Orowan process which describes the interactions between the second particles and by [75].

$$\sigma_{\text{Orowan}} = \frac{0.4MGb \ln(\bar{d}/b)}{\pi(1-\nu)^{1/2} \lambda} \quad (4)$$

where M is the Taylor factor, which is 6.5 for Mg [73]; b is the Burgers vector, which is  $3.21 \times 10^{-10}$  m for Mg [73] and  $\nu$  is the Poisson's ratio (0.35) [73].  $\bar{d}$  equals  $\sqrt{2/3}d_{\text{UFG}}$  and  $\lambda$  can be rewritten as  $\bar{d}(\sqrt{\pi/4f} - 1)$ . f represents the volume fraction of the second-phase particles, which is 0.16 and 0.13 for the as-sprayed-ECAP and as-cast-ECAP samples. The YS increase of 88 and 70 MPa for the as-sprayed-ECAP and as-cast-ECAP samples, respectively, are attributed to the second-phase particle strengthening.

Dislocation strengthening can be calculated on the basis of the Taylor formula [76].

$$\tau = CGb\rho^{1/2} \quad (5)$$

where  $\rho$  is the density of dislocations, C is a constant assumed to be 0.3 by Ashby [77]. Using the relationship of threefold between the normal stress  $\sigma$  and shear stress  $\tau$ , the YS has increased by 21 MPa and 16 MPa, respectively, due to the dislocation strengthening.

Table 5 compares different strengthening contributions: after ECAP processing, the second-phase particle strengthening contributes about 55% of the overall strength, which can be ascribed to the advantageous distributions and morphologies of  $\beta$ -Mg<sub>17</sub>Al<sub>12</sub> particles. The grain refinement and dislocation strengthening contributions are about 20% and 15%, respectively. However, because of depletion of Al to form Mg<sub>17</sub>Al<sub>12</sub> particles, the contribution of solid solution strengthening decreases by about 10%.

## 5. Conclusions

In this study, we synthesized CG AZ80 Mg alloys by casting and spray forming, followed by extrusion and ECAP at different temperatures. The sample prepared by spray forming and ECAP process has a yield strength of 235 MPa and a tensile elongation to failure of 14%, which are much larger than their conventional counterparts (with yield strength-elongation to failure combinations of 140 MPa-5%). Microstructure investigations revealed that

the excellent strength and ductility combination is attributed to a unique bi-modal structure: coarse Mg grains were separated and surrounded by deformation networks consisting of ultrafine grained Mg and ellipsoidal shaped  $\beta$ -Mg<sub>17</sub>Al<sub>12</sub> particles. Such a unique microstructure is believed to produce high back stress and back stress hardening to enhance both the strength and ductility. The Mg<sub>17</sub>Al<sub>12</sub> second-phase strengthening made greatest contribution to the yield strength. This work indicates that the combination ECAP processing with spray forming can dramatically improve the mechanical properties of AZ80 Mg alloys.

## Acknowledgements

The authors gratefully acknowledge financial support of Program for New Century Excellent Talents in University from Chinese Ministry of Education, National Natural Science Foundation of China (51225102 and 2012CB932203). The 8th "Liu da Ren cai Gao feng B932203" from Jiangsu Province, China, and the Jiangsu Key Laboratory of Advanced Nanomaterials and Technologies. SEM, TEM and X-ray were performed in the Materials Characterization Facility of the Nanjing University of Science and Technology. R.K. would like to acknowledge the support provided by the Russian Ministry of Education and Science within the basic part of the program for universities supported by the Russian Ministry for Education and Science (RZV through the Grant No 14.B25.31.0017). E.J.L. acknowledge the support from National Science Foundation of the United States (CMMI-1631873 NSF-CMMI-1437327). Y.T.Z. acknowledge the support of the China 1000Plan program and the U.S. Army Research Office (W911NF-12-1-0009).

## References

- [1] A.A. Luo, J. Magnes. Alloy. 1 (2013) 2–22.
- [2] R.Z. Valiev, R.K. Islamgaliev, I.V. Alexandrov, Prog. Mater. Sci. 45 (2000) 103–189.
- [3] M. Lalpoor, J. Dzwonczyk, N. Hort, S. Offerman, J. Alloy. Compd. 557 (2013) 73–76.
- [4] J. Chen, Y. Song, D. Shan, E.H. Han, Corros. Sci. 93 (2015) 90–99.
- [5] T. Laha, Y. Chen, D. Lahiri, A. Agarwal, Compos. Part A: Appl. Sci. Manuf. 40 (2009) 589–594.
- [6] J. Mi, P. Grant, Acta Mater. 56 (2008) 1588–1596.
- [7] R.A. Mesquita, C.A. Barbosa, Mater. Sci. Eng.: A 383 (2004) 87–95.
- [8] G. Antipas, C. Lekakou, P. Tsakirooulos, Mater. Charact. 62 (2011) 402–408.
- [9] B.Q. Han, E.J. Lavernia, F.A. Mohamed, Metall. Mater. Trans. A 36 (2005) 345–355.
- [10] L. Lu, L.G. Hou, J.X. Zhang, H.B. Wang, H. Cui, J.F. Huang, Y.A. Zhang, J.S. Zhang, J. Mater. Res. (2016) 1–7.
- [11] Z. Li, X. Yang, J. Zhang, B. Zheng, Y. Zhou, A. Shan, E.J. Lavernia, Metall. Mater. Trans. A 45 (2014) 5017–5028.
- [12] J. Schreiber, Z. Omcikus, T. Eden, M. Sharma, V. Champagne, S. Patankar, J. Alloy. Compd. 617 (2014) 135–139.
- [13] D.Y. Yang, W.Y. Xu, Z. Li, G.Q. Zhang, Z.L. Ning, J.F. Sun, Mater. Sci. Forum (2013) 564–568.
- [14] C. Chen, C.Y. Tsao, Mater. Sci. Eng.: A 383 (2004) 21–29.
- [15] X.F. Wang, J.Z. Zhao, J. He, Z.Q. Hu, Trans. Nonferrous Met. Soc. China 17 (2007) 238–243.
- [16] Y.T. Zhu, T.C. Lowe, Mater. Sci. Eng.: A 291 (2000) 46–53.

- [17] C. Howard, D. Frazer, A. Lupinacci, S. Parker, R. Valiev, C. Shin, B.W. Choi, P. Hosemann, *Mater. Sci. Eng.: A* 649 (2016) 104–113.
- [18] Y.H. Zhao, X.Z. Liao, Y.T. Zhu, R.Z. Valiev, *J. Mater. Res.* 20 (2005) 288–291.
- [19] A.V. Polyakov, I.P. Semenova, Y. Huang, R.Z. Valiev, T.G. Langdon, *Adv. Eng. Mater.* 16 (2014) 1038–1043.
- [20] V.G. Pushin, R.Z. Valiev, Y.T. Zhu, D.V. Gunderov, N.I. Kourov, T.E. Kuntsevich, A. N. Uksusnikov, L.I. Yurchenko, *Mater. Trans.* 47 (2006) 694.
- [21] J. Suh, J. Victoria-Hernández, D. Letzig, R. Golle, W. Volk, *Mater. Sci. Eng.: A* 650 (2016) 523–529.
- [22] C. Haase, O. Kremer, W. Hu, T. Ingendahl, R. Lapovok, D.A. Molodov, *Acta Mater.* 107 (2016) 239–253.
- [23] H. Liu, Z. Sun, G. Wang, X. Sun, J. Li, F. Xue, H. Peng, Y. Zhang, *Mater. Sci. Eng.: A* 654 (2016) 107–112.
- [24] X. Yang, H. Miura, T. Sakai, *Mater. Des.* 44 (2013) 573–579.
- [25] Y. Miyahara, Z. Horita, T.G. Langdon, *Mater. Sci. Eng.: A* 420 (2006) 240–244.
- [26] W. Kim, J. Park, W. Kim, *J. Alloy. Compd.* 460 (2008) 289–293.
- [27] A. Yamashita, Z. Horita, T.G. Langdon, *Mater. Sci. Eng.: A* 300 (2001) 142–147.
- [28] F. Lu, A. Ma, J. Jiang, D. Yang, Y. Yuan, L. Zhang, *J. Alloy. Compd.* 601 (2014) 140–145.
- [29] X. Yang, H. Miura, T. Sakai, *Mater. Trans.* 46 (2005) 2981–2987.
- [30] H. Kitahara, F. Maruno, M. Tsushida, S. Ando, *Mater. Sci. Eng.: A* 590 (2014) 274–280.
- [31] P. Wang, F.Y. Han, Y.S. Wang, L. Geng, S.F. Meng, W. Liang, *Adv. Mater. Res.* 602 (2013) 602–607.
- [32] H. Jafarzadeh, K. Abrinia, A. Babaei, *Mater. Sci. Eng.: A* 596 (2014) 194–199.
- [33] H. Wang, K. Zhou, G. Xie, X. Liang, W. Liang, Y. Zhao, *Mater. Sci. Eng.: A* 560 (2013) 787–791.
- [34] B. Chen, D.L. Lin, L. Jin, X.Q. Zeng, C. Lu, *Mater. Sci. Eng.: A* 483 (2008) 113–116.
- [35] A.S.H. Kabir, J. Su, S. Yue, *Metall. Mater. Trans. B* (2016) 1–7.
- [36] S.M. Arab, A. Akbarzadeh, *J. Magnes. Alloy.* 2 (2014) 203–207.
- [37] R. Jahadi, M. Sedighi, H. Jahed, *Mater. Sci. Eng.: A* 593 (2014) 178–184.
- [38] R.B. Figueiredo, T.G. Langdon, *Mater. Sci. Eng.: A* 501 (2009) 105–114.
- [39] T. Mukai, M. Yamanoi, H. Watanabe, K. Higashi, *Scr. Mater.* 45 (2001) 89–94.
- [40] H. Lin, J. Huang, T. Langdon, *Mater. Sci. Eng.: A* 402 (2005) 250–257.
- [41] D. Foley, M. Al-Maharbi, K. Hartwig, I. Karaman, L. Kecskes, S. Mathaudhu, *Scr. Mater.* 64 (2011) 193–196.
- [42] M. Bleckmann, M. Eichhorst, M. Schuch, W. Kreuzer, V. Hammond, C. Spiller, L. Meyer, N. Herzig, *Mater. Sci. Eng.: A* 660 (2016) 108–117.
- [43] P. Molnár, A. Jäger, *Philos. Mag.* 93 (2013) 3612–3626.
- [44] S. Biswas, S. Singh Dhinwal, S. Suwas, *Acta Mater.* 58 (2010) 3247–3261.
- [45] Z. Zhang, S.K. Vajpai, D. Orlov, K. Ameyama, *Mater. Sci. Eng.: A* 598 (2014) 106–113.
- [46] S. Celotto, *Acta Mater.* 48 (2000) 1775–1787.
- [47] A. Dhar, R. Anandani, A. Srivastava, *Mater. Sci. Technol.* 27 (2011) 1275–1280.
- [48] A. Vinogradov, D. Orlov, A. Danyuk, Y. Estrin, *Acta Mater.* 61 (2013) 2044–2056.
- [49] Z. Li, A. Luo, Q. Wang, L. Peng, P. Fu, G. Wu, *Mater. Sci. Eng.: A* 564 (2013) 450–460.
- [50] S. Ding, W. Lee, C. Chang, L. Chang, P. Kao, *Scr. Mater.* 59 (2008) 1006–1009.
- [51] H.K. Kim, Y.-I. Lee, C.-S. Chung, *Scr. Mater.* 52 (2005) 473–477.
- [52] W.J. Kim, H.T. Jeong, *Mater. Trans.* 46 (2005) 251–258.
- [53] Z. Zúberová, L. Kunz, T. Lamark, Y. Estrin, M. Janeček, *Metall. Mater. Trans. A* 38 (2007) 1934–1940.
- [54] H. Somekawa, T. Mukai, *Scr. Mater.* 54 (2006) 633–638.
- [55] C. Su, B. Chua, L. Lu, M. Lai, *Mater. Sci. Eng.: A* 402 (2005) 163–169.
- [56] H.K. Kim, *Mater. Sci. Eng.: A* 515 (2009) 66–70.
- [57] S.Y. Chang, S.W. Lee, K.M. Kang, S. Kamado, Y. Kojima, *Mater. Trans.* 45 (2004) 488–492.
- [58] W. Kim, Y. Sa, *Scr. Mater.* 54 (2006) 1391–1395.
- [59] S. Agnew, J. Horton, T. Lillo, D. Brown, *Scr. Mater.* 50 (2004) 377–381.
- [60] W. Kim, C. An, Y. Kim, S. Hong, *Scr. Mater.* 47 (2002) 39–44.
- [61] W. Kim, S. Hong, Y. Kim, S. Min, H. Jeong, J. Lee, *Acta Mater.* 51 (2003) 3293–3307.
- [62] J. Jiang, Y. Wang, J. Qu, *Mater. Sci. Eng.: A* 560 (2013) 473–480.
- [63] Y. Chino, M. Mabuchi, *Adv. Eng. Mater.* 3 (2001) 981–983.
- [64] K. Máthys, J. Gubicza, N. Nam, *J. Alloy. Compd.* 394 (2005) 194–199.
- [65] T.S. Pereira, C.W. Chung, R. Ding, Y.L. Chiu, *IOP Conf. Ser.: Mater. Sci. Eng.* (2009) 012022.
- [66] P. Mehrotra, T. Lillo, S. Agnew, *Scr. Mater.* 55 (2006) 855–858.
- [67] B. Shi, R. Chen, W. Ke, *Mater. Sci. Eng.: A* 546 (2012) 323–327.
- [68] X.L. Wu, M.X. Yang, F.P. Yuan, G.L. Wu, Y.J. Wei, X.X. Huang, Y.T. Zhu, *Proc. Natl. Acad. Sci.* 112 (2015) 14501–14505.
- [69] M.X. Yang, Y. Pan, F.P. Yuan, Y.T. Zhu, X.L. Wu, *Mater. Res. Lett.* (2016) 1–7.
- [70] G. Liu, G. Zhang, F. Jiang, X. Ding, Y. Sun, J. Sun, E. Ma, *Nat. Mater.* 12 (2013) 344–350.
- [71] Y.H. Zhao, X.Z. Liao, Z. Jin, R.Z. Valiev, Y.T. Zhu, *Acta Mater.* 52 (2004) 4589–4599.
- [72] C. Caceres, D. Rovera, *J. Light Met.* 1 (2001) 151–156.
- [73] R. Armstrong, I. Codd, R. Douthwaite, N. Petch, *Philos. Mag.* 7 (1962) 45–58.
- [74] R.W. Hertzberg, R.P. Vinci, J.L. Hertzberg, *Deformation and Fracture Mechanics of Engineering Materials*, Wiley, New York, 1996.
- [75] L. Brown, R. Ham, A. Kelly, R. Nicholson, *Applied Science*, London, 1971, p. 9.
- [76] M.F. Ashby, *Philos. Mag.* 21 (1970) 399.
- [77] N. Fleck, G. Muller, M. Ashby, J. Hutchinson, *Acta Metall. Mater.* 42 (1994) 475–487.